



Multifunctional electrocatalyst PtM with low Pt loading and high activity towards hydrogen and oxygen electrode reactions: A computational study

Xingshuai Lv, Wei Wei*, Hao Wang, Baibiao Huang, Ying Dai*

School of Physics, State Key Laboratory of Crystal Materials, Shandong University, 250100, Jinan, China

ARTICLE INFO

Keywords:

multifunctional electrocatalyst
Pt monolayer
HER
OER
ORR

ABSTRACT

Multifunctional electrocatalysts (MFEs) for hydrogen evolution reaction (HER), oxygen evolution reaction (OER) and oxygen reduction reaction (ORR) are highly desirable for the development of electrochemical systems including water electrolysis, fuel cells and metal–air batteries, which have been rarely reported to date. Despite the high activity of Platinum (Pt), the limited reserves and high price severely limit its wide application. Therefore, it is urgent to explore catalysts requiring minimal amounts of Pt but still active to function. In accordance to the typical experimental electrocatalytic conditions for Pt monolayer (PtM), in this work we first identify the atomic configuration of PtM and evaluate the electronic and electrocatalytic properties towards HER, OER and ORR. Density functional theory (DFT) investigations suggest that PtM exhibits a buckled structure (*b*-PtM) and holds great promise for low-Pt-loading and, interestingly, all-in-one electrocatalyst, which could be highly active towards HER, OER and ORR. Our results show that the excellent electrocatalytic activity mainly originates from the amounts of highly active catalytic sites and low theoretical HER/OER/ORR overpotentials, even lower than those of currently commercialized Pt. Remarkably, the significantly reduced reaction barriers on *b*-PtM elucidate the fast reaction kinetics reported in experiments. Therefore, this work may stimulate the development of PtM electrocatalyst for other key energy conversion processes including oxygen evolution reaction and further breakthroughs of low-Pt-loading electrocatalysts.

1. Introduction

Electrocatalytic hydrogen evolution reaction (HER), oxygen evolution reaction (OER) and oxygen reduction reaction (ORR) are the heart of electrochemical energy conversion processes, such as hydrogen production from water electrolysis, fuel cells and rechargeable metal–air batteries [1]. Currently, noble metal-based catalysts are typically selected to achieve favorable reaction rates for these reactions, and Pt always exhibits outstanding catalytic activity among the available catalysts [2,3]. However, on account of the limited reserves and high price, it is highly demanding to design Pt catalysts with high atomic efficiency without compromising the performance of the electrochemical reactions. As alternatives, therefore, many Pt-based catalysts like metal alloys, hollow nanomaterials and core–shell nanoparticles were designed to reduce Pt loading and identified as promising catalysts for electrochemical reactions [4–10].

Recently, catalysts based on two-dimensional (2D) materials have aroused great interest owing to the high activity and large number of reaction sites [11–18]. For example, in combination with theoretical study, Seh et al. experimentally examined the potential of MXenes as

HER electrocatalysts [13]. The basal planes of Mo_2CT_x ($T_x = \text{H}, \text{O}, \text{OH}$, and H_2O) were found to be catalytically active toward the HER and exhibit the best activity therein. Inspired by the success of 2D catalysts, metal-based ultrathin catalysts have recently been synthesized, which can not only lower the metal content, but also dramatically improve the catalytic performance [19,20]. It is worth pointing out that 2D nanosheets are expected to have comparable or even larger specific surface area than nanoparticles. Furthermore, nanosheets could be more stable than nanoparticles due to the planar bonding. In 2014, Duan and co-workers fabricated single-layered Ru nanosheets and examined its catalytic activity in hydrogenation and hydroformylation [19]. Recently, Pt nanosheets, supported Pt monolayer-based catalysts, and Pt monolayer shells with core–shell nanostructures have been synthesized and attracted considerable attention. These Pt monolayer catalysts exhibit exceptional catalytic activity towards various electrochemical reactions including HER and OER. For example, Liu et al. first reported the successful synthesis of Pt monolayer and concluded that Pt monolayers can work as well as or even better than thicker Pt films for catalyzing HER [20,21]. On the other hand, as-prepared Pt monolayers also exhibit exceptional electrocatalytic performance towards ORR

* Corresponding authors.

E-mail addresses: weiw@sdu.edu.cn (W. Wei), daiy60@sdu.edu.cn (Y. Dai).

<https://doi.org/10.1016/j.apcatb.2019.05.045>

Received 28 November 2018; Received in revised form 26 April 2019; Accepted 13 May 2019

Available online 15 May 2019

0926-3373/ © 2019 Elsevier B.V. All rights reserved.

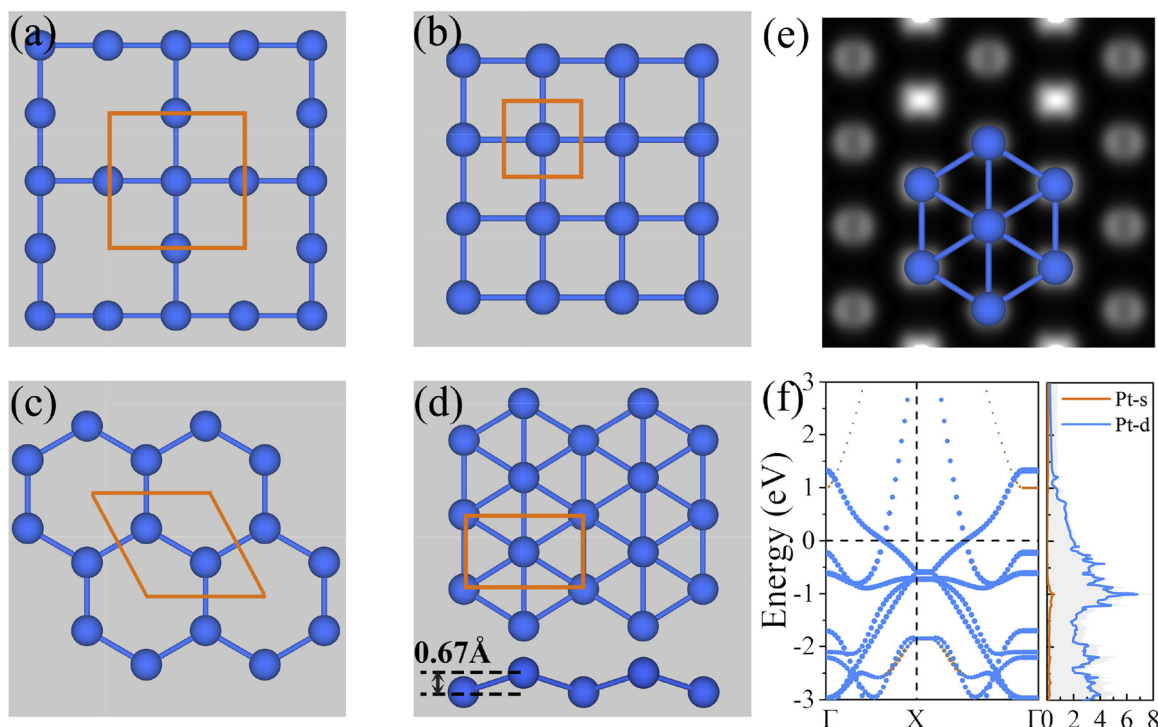


Fig. 1. Different motifs of 2D PtM, (a) tetracoordinate, (b) square, (c) honeycomb phases and (d) six-coordinated buckled PtM (*b*-PtM). (e) Simulated STM image for *b*-PtM. (f) Band structures and projected density of states (PDOS) of *b*-PtM. The Fermi level is set to zero.

[22–25]. Despite of the blossoming interest in experiments, however, there is lack of an in-depth understanding on the underlying mechanisms of the electrocatalytic performances of Pt monolayers. Thus, our results can not only advance the comprehension of monolayer metal based electrocatalysts, but also shed some light on the principles of catalyst design and the optimization of catalytic efficiency, serving as a general guideline for further breakthroughs in future.

On the other hand, the greatest strengths of MFECs lie in the reduction of product cost due to the less usage of equipment and less preparation procedures compared with separate unifunctional catalysts [26]. For overall water splitting with OER and HER occurring, bifunctional catalysts always show higher performance than two separate unifunctional catalysts, as the optimal working conditions for two unifunctional catalysts are generally not the same [26]. It will bring more interest, therefore, to design and/or development bifunctional catalysts.

In this work, for the first time, we theoretically report the excellent electrocatalytic activity of the experimentally realized Pt monolayer (PtM), which not only possesses low Pt loading, but also holds great promise to act as highly active MFECs for HER, OER and ORR. With the aid of the computational hydrogen electrode (CHE) model, we examined the reaction free energies and energy barriers of all possible elementary reactions on PtM. The prominently reduced overpotentials and activation barriers indicate that the electrocatalytic activities of PtM are far superior to the currently used Pt (111) surface.

2. Computational method

The first-principles calculations were performed using the projector augmented wave (PAW) method as implemented in the Vienna *ab initio* simulation package (VASP) [27,28]. The exchange–correlation interactions were treated by the generalized gradient approximation (GGA) in the form of the Perdew–Burke–Ernzerhof (PBE) functional [29], and a cutoff energy of 500 eV for plane-wave basis set was adopted. The convergence threshold were 10^{-5} eV and 0.01 eV/Å for energy and force, respectively. The vacuum space was at least 15 Å, which was

large enough to avoid the interactions between periodical images. To take the van der Waals (vdW) interactions into account, the dispersion corrected DFT–D2 scheme was adopted [30]. The climbing–image nudged elastic band (CI–NEB) method [31] implemented in VASP was used to determine the diffusion barrier and the minimum energy pathways for the reactions on PtM. Ab initio molecular dynamics (AIMD) simulations in NVT ensemble using Nosé heat bath method lasted for 10 ps with a time step of 1.0 fs. The electrocatalytic activity were evaluated by the reaction Gibbs free energy (ΔG) for each step via the equation

$$\Delta G = \Delta E + \Delta E_{\text{ZPE}} - T\Delta S - neU$$

where ΔE is the adsorption energy of the corresponding adsorbed intermediates, and ΔE_{ZPE} and ΔS are the difference in the zero-point energy and the change in entropy before and after adsorption, respectively. U is the electrode potential and n is the number of transferred electrons. The contributions from the catalysts to ΔE_{ZPE} and ΔS are small and thus neglected. Details for calculating the overpotentials of HER, OER and ORR are provided in the **Supporting Information (SI)**. The cohesive energy of PtM was calculated according to the equation

$$E_{\text{coh}} = (E_{\text{PtM}} - nE_{\text{Pt}})/n$$

with n being the total atom number. The adsorption energies of various intermediates can be obtained by

$$E_{\text{ads}} = E_{\text{tot}} - E_{\text{PtM}} - E_{\text{inter}}$$

where E_{tot} , E_{PtM} and E_{inter} are the total energies of the adsorbed systems, freestanding PtM and various intermediates, respectively.

3. Results and discussion

3.1. Structural and electronic properties of PtM

As shown in Figs. 1a–d, four possible forms of PtM were taken into account, namely, tetracoordinate, square, honeycomb and six-coordinated buckled PtM (*b*-PtM). With respect to the stability, cohesive

energy is a widely accepted parameter to evaluate the feasibility for experimental synthesis of the predicted 2D materials [32,33]. The cohesive energy of six-coordinated *b*-PtM was examined to be -5.18 eV/atom, which is close to that of Pt (111) surface (-5.45 eV/atom). Other motifs, such as tetracoordinate, square, and honeycomb PtM, have relatively higher cohesive energies of -3.84 , -4.67 and -4.26 eV/atom, respectively. Therefore, the six-coordinated *b*-PtM is the most stable form therein and likely to be synthesized under certain experimental conditions. The following discussion is focused on the most stable six-coordinated *b*-PtM hereafter. In analogous to silicene, the primitive cell of *b*-PtM contains two Pt atoms and the optimized lattice constants are $a = 4.20$ Å, $b = 2.62$ Å. As a reference to experimental observation about the structures, simulated scanning tunneling microscopy (STM) image of *b*-PtM is shown in Fig. 1e. The phonon dispersion (Figure S1a) shows negligible imaginary frequency from Γ to Γ point, thus *b*-PtM is dynamically stable. As indicated in Figures S1b and S1c, the smooth fluctuation of the total energy and intact structure throughout the *ab initio* molecular dynamics (AIMD) simulations demonstrate the thermal stability of *b*-PtM.

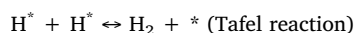
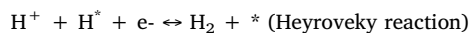
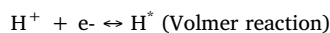
Catalytic properties are closely related to the electronic structures. The band structure and projected density of states (PDOS) in Fig. 1f show that *b*-PtM is metallic with plenty of states crossing the Fermi level, guaranteeing the electrical conductivity of the catalysts. In addition, the stability of *b*-PtM can also be explained through the PDOS. As shown in Figure S2a, the π states composed of d_{xz} and d_{yz} orbitals obviously hybridize with the σ states contributed by $d_{x^2-y^2}$ and d_{xy} orbitals, thus stabilizing the structure. Whereas, the π - σ hybridization in other forms of PtM is not significant compared to the *b*-PtM (Figures S2b-d). Therefore, similar to the buckled silicene and stanene, such an orbital hybridization could stabilize the buckled characteristics [34].

3.2. HER

In principle, an ideal HER catalyst should hold a thermal-neutral (close to 0 eV) Gibbs free energy of hydrogen adsorption ($\Delta G_{H^*} = 0$ eV) [35–39]. Regarding *b*-PtM, there are three possible sites for hydrogen adsorption, which are labeled as T, D and H sites (see Fig. 1a). As shown in Fig. 2a, the corresponding ΔG_{H^*} (see SI) at these sites are 0.09, -0.004 , and -0.04 eV, which are even lower than currently commercialized Pt (-0.09 eV) [40]. Based on the ΔG_{H^*} and theoretical exchange current i_0 , the volcano curve for comparing the HER activity of *b*-PtM with Nb, Pt, Pd, Cu, Ag, N-doped graphene and MoS₂ is shown in Fig. 2b. The HER performance of catalysts can be evaluated by their i_0 position relative to the volcano peak, which is defined as the preferred catalytic region. It can be observed that Nb, Cu, Ag, N-doped graphene and MoS₂ exhibit either too negative or too positive ΔG_{H^*} , which are not beneficial for releasing or adsorbing H during the HER

process. In contrast, Pt and Pd are suitable HER catalysts with ΔG_{H^*} located close to the ideal region ($\Delta G_{H^*} = 0$). Especially, the lowest i_0 of *b*-PtM indicates the best HER performance. In experiments, the polarization curve (see SI) is one of the most persuasive parameters to quantify the HER activity, and the lower the required potential to achieve 10 mA/cm^2 current density (i) is, the better the HER activity is [39]. As shown in Fig. 2c, current Pt already shows a low potential of -58 meV , though, the required potential for *b*-PtM could be as low as -10 meV , indicating a superior HER activity.

As schematically shown in Figs. 3a and 3b, HER after hydrogen adsorption (Volmer reaction) proceeds in acid media following either the Heyrovsky or the Tafel reaction:



According to the activation barriers in Figs. 3c–3e, hydrogen evolution on *b*-PtM tends to follow Volmer–Heyrovsky (0.29 eV) rather than the Volmer–Tafel (0.53 eV) reaction. Low activation barrier thereby indicates a fast HER rate of *b*-PtM. In virtue of the low overpotential and fast kinetics, *b*-PtM is an attractive candidate for HER electrocatalysts with minimal Pt usage, illuminating the high-activity including low overpotential of Pt monolayer fabricated in the experiments [20,21].

3.3. OER

In acidic environment, a complete OER includes four elementary steps: (1) H₂O molecule dissociates into HO^{*}; (2) HO^{*} further dissociates into O^{*}; (3) O^{*} reacts with another H₂O molecule and produces HOO^{*}; (4) the final product O₂ forms and is then released. The details for OER are shown in the SI. In every elementary step, the release of a H⁺ cation and an electron always occurs. Figs. 4a–4e show the adsorption configurations of all the possible OER intermediate species (HO^{*}, O^{*}, HOO^{*}) on *b*-PtM, and the preferred adsorption sites along with their binding energies are listed in Table 1. For comparison, the case for Pt (111) surface is also given [41]. The overpotential of OER (η^{OER}) can be obtained based on the Gibbs free energy of each elementary step (see details in SI). As shown in Fig. 4f, the OER is uphill when the electrode potential (U) is 0 V. At $U = 1.23$ V, steps (1), (2) and (4) become downhill, but step (3) is still uphill. Only when the applied potential increases to 1.96 V, all the elementary reaction steps can become downhill. Therefore, the overpotential η^{OER} turns out to be 0.71 V ($\eta^{\text{OER}} = 1.94 - 1.23$ V) and the transformation of O^{*} \rightarrow HOO^{*} is the rate-determining step. In this case, the η^{OER} of *b*-PtM is comparable to or even lower than those of other extensively studied catalysts, such as

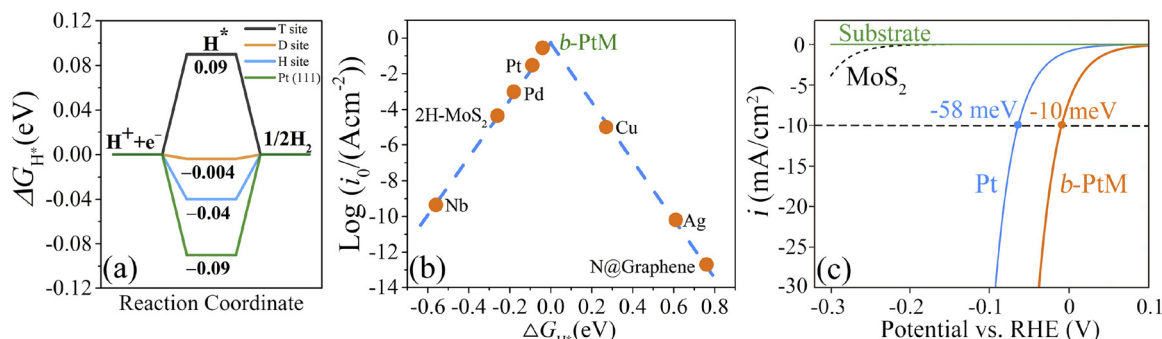


Fig. 2. (a) Free energy diagram for hydrogen evolution on different active sites at potential $U = 0$ relative to the standard hydrogen electrode at pH = 0. (b) Volcano curve of exchange current density i_0 as a function of the Gibbs free energy (ΔG_{H^*}). For comparison, other widely studied HER electrocatalysts are also shown, including Nb, Pd, Pt, Cu, Ag, N-doped graphene (N@Graphene) and 2H-MoS₂. (c) Predicted current density of *b*-PtM versus other HER electrocatalysts. *b*-PtM shows lower required potential (-10 meV) than Pt (-58 meV) to achieve the current density of 10 mA/cm^2 , indicating a superior HER activity, while MoS₂ has low HER activity owing to the high potential.

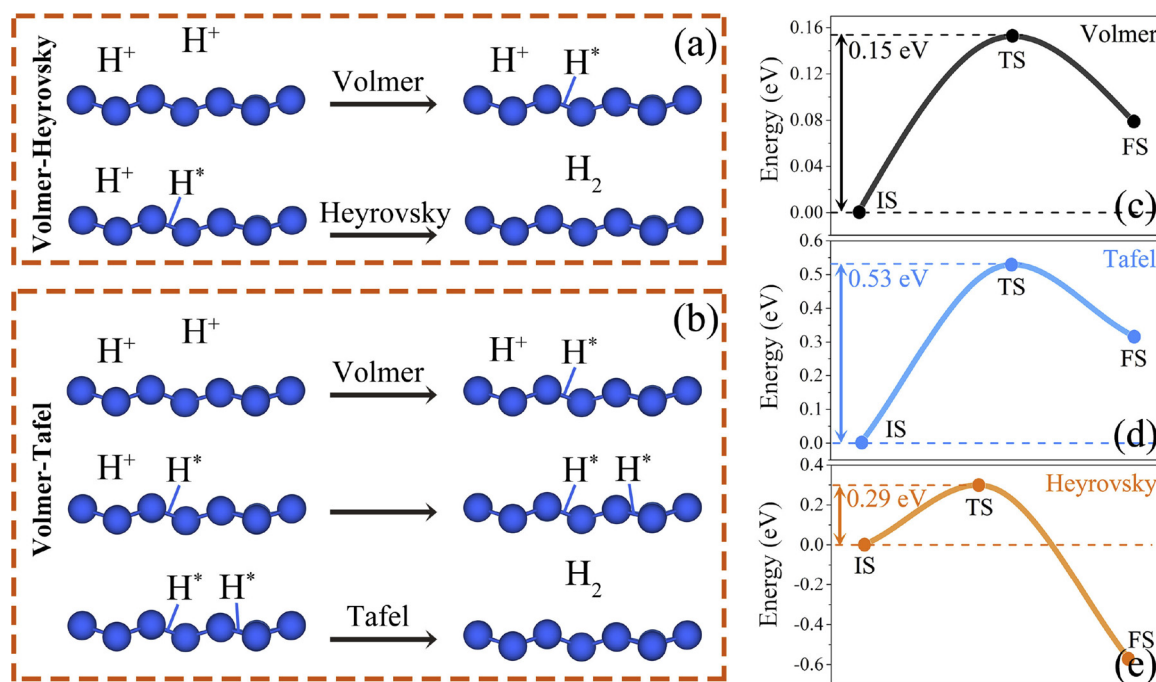


Fig. 3. HER Pathways of (a) Volmer–Heyrovsky and (b) Volmer–Tafel reactions. Corresponding activation barriers for (c) Volmer, (d) Tafel and (e) Heyrovsky reactions.

metal atoms decorated boron monolayer (0.40 – 2.16 eV) and Pt (111) surface (0.76 eV) [26,42,43].

To intuitively compare the OER performance of *b*-PtM with other catalysts, the OER volcano curve is plotted and the detailed calculation method is provided in the SI. In general, the binding strength of the intermediates (HO^* , O^* and HOO^*) on catalysts determines the energetics and hence the rates of the OER. Either too strong or too weak adsorption can impair the OER activity. Therefore, three descriptors including ΔG_{HOO^*} , ΔG_{O^*} and ΔG_{HO^*} are required to evaluate the OER activity of the catalysts. By fitting the ΔG_{HO^*} and ΔG_{HOO^*} of *b*-PtM, metal atoms decorated boron monolayer and Pt (111), as shown in Figure S3, the relationship between ΔG_{HO^*} and ΔG_{HOO^*} can be established and expressed as $\Delta G_{\text{HOO}^*} = 0.85\Delta G_{\text{HO}^*} + 3.11$ eV. Fig. 4g shows the theoretical volcano curve with ΔG_{HO^*} and $(\Delta G_{\text{O}^*} - \Delta G_{\text{HO}^*})$ as

Table 1

Preferred adsorption sites and binding energies (eV) of various OER/ORR intermediate species on *b*-PtM and Pt (111) surface. Here, B, H, T and F denote bridge, hollow, top and *fcc* sites, respectively.

	O_2^*	O^*	HO^*	HOO^*	H_2O_2^*
<i>b</i> -PtM	−0.62 (B)	−4.49 (H)	−2.29 (B)	−1.08 (B)	−0.12 (B)
Pt (111)	−0.67 (B)	−4.42 (F)	−2.34 (T)	−1.12 (B)	−0.30 (B)

descriptors, which is divided into four zones based on the rate-determining step. For Ti deposited borophene β_{12} ($\text{Ti-}\beta_{12}$), the interaction between HO^* and $\text{Ti-}\beta_{12}$ is too strong with a very negative ΔG_{HO^*} and results in a very positive ΔG_4 . So step (4) (zone 4) turns out to be the rate-determining step for $\text{Ti-}\beta_{12}$ with a high overpotential of 2.12 V.

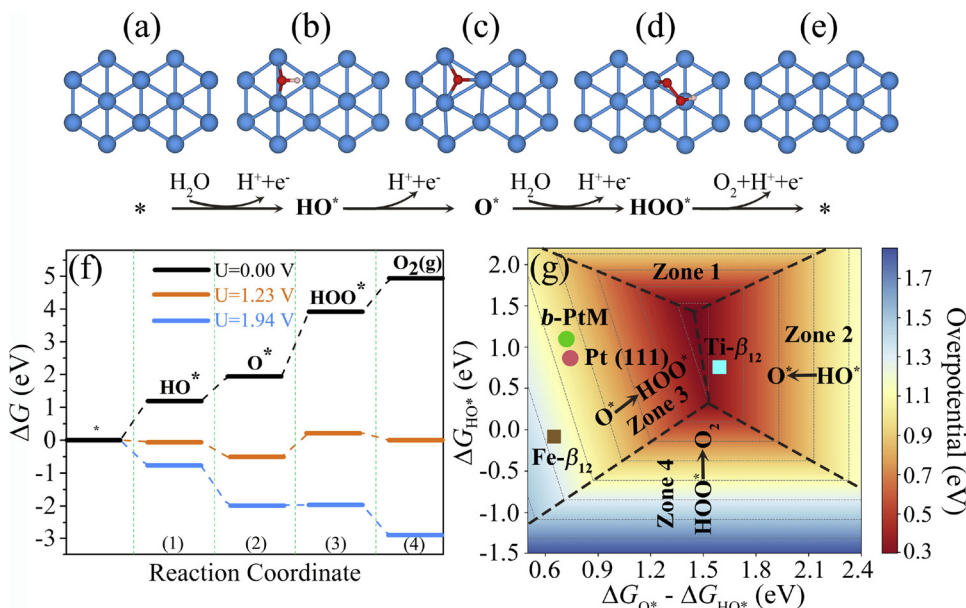
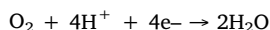


Fig. 4. (a–e) Adsorption configurations and OER pathways of intermediates HO^* , O^* and HOO^* on *b*-PtM. (f) Free energy diagrams of OER on *b*-PtM at different electrode potential *U*. (g) OER activity volcano showing the overpotential as a function of Gibbs free energies of the reaction intermediates. Color bar represents the value of OER overpotential. The black dashed lines divide the 3D activity volcano into four zones based on the potential-determining step.

Similarly, step (3) (zone 3) is the rate-determining step for Fe deposited borophene β_{12} (Fe- β_{12}) (with an overpotential of 1.31 V), Pt (111) and *b*-PtM. Obviously, *b*-PtM shows the impressively low overpotential of 0.71 V.

3.4. ORR

As a major determining factor for the performance of fuel cells and metal–air batteries, the cathodic ORR plays a vital role in electricity production. Along with the $4e^-$ pathway, the total ORR in the acidic environment could be expressed as



According to the feasibility of O–O bond dissociation, two possible reaction mechanisms, namely, direct and indirect processes should be taken into account in the acidic environment. In the case of the direct pathway, O–O bond dissociation (2O^*) is favorable, whereas O_2^* hydrogenation (HOO^*) tends to occur in the indirect pathway. The detailed reaction processes are shown in the SI.

Therefore, the dissociation of oxygen molecule is a precondition to the subsequent ORR pathways. For *b*-PtM, oxygen molecule can be spontaneously adsorbed with an adsorption energy of -0.68 eV. Compared with the bond length of gaseous O_2 (1.23 Å), the bond length of adsorbed oxygen molecule (O_2^*) is obviously stretched to 1.28 Å. As shown in Figure S4, O_2^* can directly dissociate into two adsorbed O atoms (O^*) with a reaction barrier of 0.28 eV, which is much lower than that on Pt (111) surface (0.53 eV).⁴⁰ In addition, barrier of O_2^* hydrogenation on *b*-PtM was evaluated to be 0.10 eV, which is still lower than that on Pt (111) surface (0.36 eV) [44]. Thus, *b*-PtM is more reactive towards O_2 hydrogenation (the indirect pathway) than Pt (111). In addition, the formation of HOO^* on *b*-PtM further elongates the O–O bond length to 1.42 Å, promising an easier dissociation of O–O bond for the subsequent steps.

For $\text{HOO}^* \rightarrow \text{O}^* + \text{HO}^*$ on *b*-PtM, as shown in Fig. 5a, the reaction is exothermic by -0.79 eV with a barrier of 0.02 eV. With respect to $\text{HOO}^* + (\text{H}^+ + e^-) \rightarrow \text{H}_2\text{O}_2^*$, the reaction is also exothermic by -0.69 eV with a barrier of 0.08 eV. Previous studies reported the activation barriers of 0.12 eV and 0.19 eV on Pt (111) surface for these two reactions, respectively [45,46], which are higher than those on *b*-PtM. After the HOO^* dissociation to O^* and HO^* , the adsorbed HO^* undergoes protonation and results in the formation of H_2O with a barrier of 0.02 eV, which is much lower than that on Pt (111) surface (0.16 eV) [44]. The following $\text{O}^* + \text{H}^+ + e^- \rightarrow \text{HO}^*$ on *b*-PtM is

exergonic (-0.76 eV) with a barrier of 0.12 eV. Compared to Pt (111) surface with the barrier of 0.86 eV [44], the unique buckling nature endows *b*-PtM advantages in ORR activity. On the other hand, it is noteworthy that H_2O_2^* cannot be adsorbed stably on *b*-PtM since the interaction between H_2O_2^* and *b*-PtM directly leads to the spontaneous dissociation into two HO^* , which is indicated by the large O–O bond length of 1.46 Å in H_2O_2^* .

Fig. 5b shows the effect of electrode potentials on the ORR process. When the electrode potential is zero ($U = 0$ V), all the elementary reactions of the ORR on *b*-PtM are downhill, implying that the reactions are facile. However, with the increase of electrode potential, the protonation reactions become less exothermic and some elementary steps turn out to be uphill. In particular, at $U = 0.50$ V, the protonation step ($\text{O}_2^* + \text{H}^+ + e^- \rightarrow \text{HOO}^*$) becomes endothermic. Thus, the rate-limiting step is the reduction of O_2^* to HOO^* with ORR overpotential of 0.73 V ($\eta_{\text{ORR}} = U_0 - U = 1.23 - 0.50 = 0.73$ V), which is comparable or even lower than those of Pt-based and graphene supported single-atom electrocatalysts [44,47,48]. At equilibrium potential $U = 1.23$ V, the protonation reactions become endothermic except for step (2) ($\text{HOO}^* + \text{H}^+ + e^- \rightarrow \text{O}^* + \text{H}_2\text{O}$), indicating that the electrode potential has inconspicuous influence on HOO^* protonation on *b*-PtM. This is also correct for the H_2O_2^* dissociation pathway as shown in Figure S5. Consequently, our potential-dependent study shows that *b*-PtM catalyzed ORR is thermodynamically favorable at 0.50 V and thus lowers the overpotential. Besides, kinetics analysis indicates that *b*-PtM is a very selective and efficient catalyst for H_2O formation over H_2O_2 due to the reduced reaction barriers, thus explaining the origin of experimentally reported fast ORR kinetics of as-synthesized Pt monolayer.

4. Conclusion

In conclusion, for the first time, we theoretically shed fresh light on the origin of excellent electrocatalytic activity of already-synthesized PtM by using DFT calculations. Low Pt loading and high stability lay the foundation for PtM to act as highly active multifunctional electrocatalysts toward HER, OER and ORR. Accordingly, we ascertained the most stable phase of PtM (i.e. *b*-PtM), and systemically performed electronic and electrocatalytic investigations towards HER, OER and ORR. Our state-of-the-art computational results elucidate that the cohesive energy of *b*-PtM (-5.18 eV/atom) is comparable to that of Pt (111) surface (-5.45 eV/atom), confirming the excellent stability and experimental feasibility of *b*-PtM. Besides, we found that the superior catalytic activity of *b*-PtM is derived from the large number of active

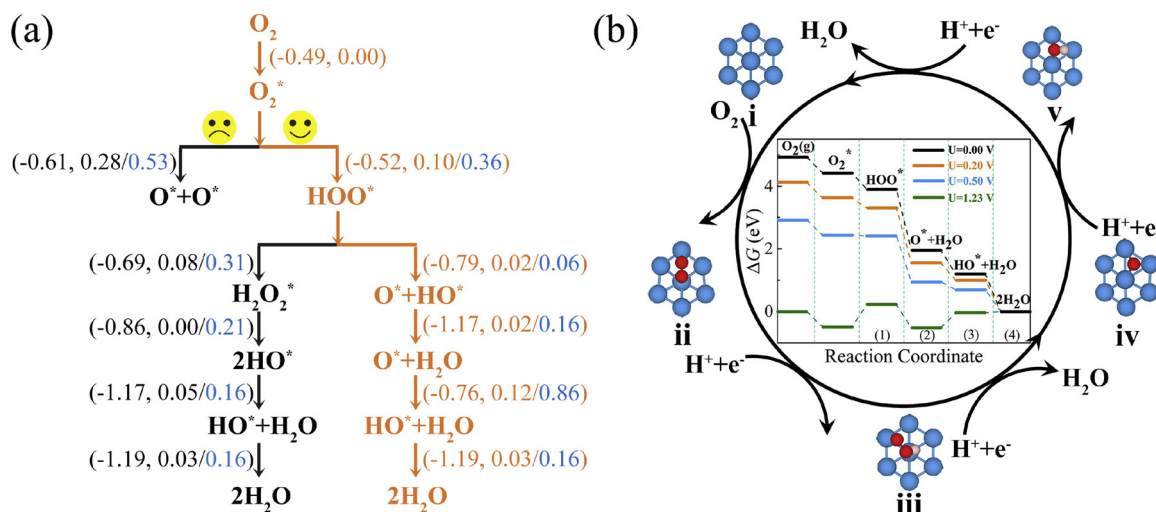


Fig. 5. (a) Possible reaction pathways for ORR on *b*-PtM. Gibbs free energies and activation energies are given for *b*-PtM, and the corresponding activation barriers are compared with those on Pt (111), energies are given in the form of (ΔG , E_a/E_a of *b*-PtM/Pt (111)). The kinetically favorable pathway is marked in orange. (b) The optimal reaction pathways for ORR on *b*-PtM at different electrode potential U .

sites, desirable electrical conductivity, low overpotentials and fast reaction kinetics, which are theoretically even better than those of Pt. Therefore, this study not only unravels the intrinsic mechanisms of experimental results, but also paves a new way for rational design of multifunctional electrocatalysts with low Pt loading.

Acknowledgements

This work is supported by the National Natural Science foundation of China (No. 51872170, 11374190 and 21333006), the Taishan Scholar Program of Shandong Province and the Young Scholars Program of Shandong University (YSPSDU).

Appendix A. Supplementary data

Supplementary material related to this article can be found, in the online version, at doi:<https://doi.org/10.1016/j.apcatb.2019.05.045>.

References

- [1] Y. Zheng, Y. Jiao, Y. Zhu, Q. Cai, A. Vasileff, L.H. Li, Y. Han, Y. Chen, S.-Z. Qiao, Molecule-level g-C₃N₄ coordinated transition metals as a new class of electrocatalysts for oxygen electrode reactions, *J. Am. Chem. Soc.* 139 (2017) 3336–3339.
- [2] J.K. Nørskov, C.H. Christensen, Toward efficient hydrogen production at surfaces, *Science* 312 (2006) 1322–1323.
- [3] J. Wang, M. Xu, J. Zhao, H. Fang, Q. Huang, W. Xiao, T. Li, D. Wang, Anchoring ultrafine Pt electrocatalysts on TiO₂-C via photochemical strategy to enhance the stability and efficiency for oxygen reduction reaction, *Appl. Catal. B: Environ.* 237 (2018) 228–236.
- [4] J.R.C. Salgado, E. Antolini, E.R. Gonzalez, Carbon supported Pt–Co alloys as methanol-resistant oxygen-reduction electrocatalysts for direct methanol fuel cells, *Appl. Catal. B: Environ.* 57 (2005) 283–290.
- [5] J. Ryu, J. Choi, D.-H. Lim, H.-L. Seo, S.-Y. Lee, Y. Sohn, J.H. Park, J.H. Jang, H.-J. Kim, S.A. Hong, P. Kim, S.J. Yoo, Morphology-controlled synthesis of ternary Pt–Pd–Cu alloy nanoparticles for efficient electrocatalytic oxygen reduction reactions, *Appl. Catal. B: Environ.* 174–175 (2015) 526–532.
- [6] N.N. Kariuki, W.J. Khudhayer, T. Karabacak, D.J. Myers, GLAD Pt–Ni alloy nanorods for oxygen reduction reaction, *ACS Catal.* 3 (2013) 3123–3132.
- [7] Y. Xiong, Y. Yang, F.J. DiSalvo, H.D. Abruna, Pt-decorated composition-tunable Pd–Fe@Pd/C core–shell nanoparticles with enhanced electrocatalytic activity towards the oxygen reduction reaction, *J. Am. Chem. Soc.* 140 (2018) 7248–7255.
- [8] H.-C. Tsai, Y.-C. Hsieh, T.H. Yu, Y.-J. Lee, Y.-H. Wu, B.V. Merinov, P.-W. Wu, S.-Y. Chen, R.R. Adzic, W.A. Goddard, DFT study of oxygen reduction reaction on Os/Pt core–shell catalysts validated by electrochemical experiment, *ACS Catal.* 5 (2015) 1568–1580.
- [9] H.-Y. Park, J.H. Park, S.J. Yoo, Hollow PdCu₂@Pt core@shell nanoparticles with ordered intermetallic cores as efficient and durable oxygen reduction reaction electrocatalysts, *Appl. Catal. B: Environ.* 225 (2018) 84–90.
- [10] K.A. Kuttilyel, Y. Choi, K. Sasaki, D. Su, S.-M. Hwang, S.-D. Yim, T.-H. Yang, G.-G. Park, R.R. Adzic, *Nano Energy* 29 (2016) 261–267.
- [11] X. Lv, W. Wei, Q. Sun, F. Li, B. Huang, Y. Dai, Two-dimensional germanium monochalcogenides for photocatalytic water splitting with high carrier mobility, *Appl. Catal. B: Environ.* 217 (2017) 275–284.
- [12] Y. Wei, Y. Ma, W. Wei, M. Li, B. Huang, Y. Dai, Promising Photocatalysts for Water Splitting in BeN₂ and MgN₂ Monolayers, *J. Phys. Chem. C* 122 (2018) 8102–8108.
- [13] Z.W. Seh, K.D. Fredrickson, A. Anasori, J. Kibsgaard, A.L. Strickler, M.R. Lukatskaya, Y. Gogotsi, T.F. Jaramillo, A. Vojvodic, Two-dimensional molybdenum carbide (MXene) as an efficient electrocatalyst for hydrogen evolution, *ACS Energy Lett.* 1 (2016) 589–594.
- [14] G. Gao, A.P. O'Mullane, A. Du, 2D MXenes: A new family of promising catalysts for the hydrogen evolution reaction, *ACS Catal.* 7 (2017) 494–500.
- [15] X. Liu, P. Wang, H. Zhai, Q. Zhang, B. Huang, Z. Wang, Y. Liu, Y. Dai, X. Qin, X. Zhang, Synthesis of synergetic phosphorus and cyano groups (–C≡N) modified g-C₃N₄ for enhanced photocatalytic H₂ production and CO₂ reduction under visible light irradiation, *Appl. Catal. B: Environ.* 232 (2018) 521–530.
- [16] X. Li, Y. Dai, M. Li, W. Wei, B. Huang, Stable Si-based pentagonal monolayers: high carrier mobilities and applications in photocatalytic water splitting, *J. Mater. Chem. A* 3 (2015) 24055–24063.
- [17] P. Zhao, Y. Ma, X. Lv, M. Li, B. Huang, Y. Dai, Two-dimensional III₂–VI₃ materials: Promising photocatalysts for overall water splitting under infrared light spectrum, *Nano Energy* 51 (2018) 533–538.
- [18] S. Wang, P. He, L. Jia, M. He, T. Zhang, F. Dong, M. Liu, H. Liu, Y. Zhang, C. Li, J. Gao, L. Bian, Nanocoral-like composite of nickel selenide nanoparticles anchored on two-dimensional multi-layered graphitic carbon nitride: A highly efficient electrocatalyst for oxygen evolution reaction, *Appl. Catal. B: Environ.* 243 (2019) 463–469.
- [19] H. Duan, N. Yan, R. Yu, C. Chang, G. Zhou, H. Hu, H. Rong, Z. Niu, J. Mao, H. Asakura, T. Tanaka, P.J. Dyson, J. Li, Y. Li, Ultrathin rhodium nanosheets, *Nat. Commun.* 5 (2014) 3093.
- [20] M. Li, Q. Ma, W. Zi, X. Liu, X. Zhu, S.F. Liu, Pt monolayer coating on complex network substrate with high catalytic activity for the hydrogen evolution reaction, *Sci. Adv.* 1 (2015) e1400268.
- [21] L. Pang, M. Li, Q. Ma, Y. Zhang, X. Ren, D. Zhang, S.F. Liu, Controlled Pt monolayer fabrication on complex carbon fiber structures for superior catalytic applications, *Electrochem. Acta* 222 (2016) 1522–1527.
- [22] K.A. Kuttilyel, K. Sasaki, Y. Choi, D. Su, P. Liu, R.R. Adzic, Bimetallic IrNi core platinum monolayer shell electrocatalysts for the oxygen reduction reaction, *Energy Environ. Sci.* 5 (2012) 5297–5304.
- [23] J. Zhang, Y. Mo, M.B. Vukmirovic, R. Klie, K. Sasaki, R.R. Adzic, Platinum Monolayer Electrocatalysts for O₂ Reduction: Pt Monolayer on Pd(111) and on carbon-supported Pd nanoparticles, *J. Phys. Chem. B* 108 (2004) 10955–10964.
- [24] Y. Zhang, Y.-C. Hsieh, V. Volkov, D. Su, W. An, R. Si, Y. Zhu, P. Liu, J.X. Wang, R.R. Adzic, High performance Pt monolayer catalysts produced via core-catalyzed coating in ethanol, *ACS Catal.* 4 (2014) 738–742.
- [25] G. Chen, K.A. Kuttilyel, D. Su, M. Li, C.-H. Wang, D. Buceta, C. Du, Y. Gao, G. Yin, K. Sasaki, M.B. Vukmirovic, R.R. Adzic, Oxygen reduction kinetics on Pt monolayer shell highly affected by the structure of bimetallic AuNi cores, *Chem. Mater.* 28 (2016) 5274–5281.
- [26] C. Ling, L. Shi, Y. Ouyang, X.C. Zeng, J. Wang, Nanosheet supported single-metal atom bifunctional catalyst for overall water splitting, *Nano Lett.* 17 (2017) 5133–5139.
- [27] G. Kresse, J. Furthmüller, Efficient iterative schemes for ab initio total-energy calculations using a plane-wave basis set, *Phys. Rev. B* 54 (1996) 11169–11186.
- [28] G. Kresse, D. Joubert, From ultrasoft pseudopotentials to the projector augmented-wave method, *Phys. Rev. B* 59 (1999) 1758–1775.
- [29] J.P. Perdew, M. Ernzerhof, K. Burke, Rationale for mixing exact exchange with density functional approximations, *J. Chem. Phys.* 105 (1996) 9982–9985.
- [30] S. Grimme, Accurate description of van der Waals complexes by density functional theory including empirical corrections, *J. Comput. Chem.* 27 (2006) 1787–1799.
- [31] G. Henkelman, B.P. Uberuaga, H. Jonsson, A climbing image nudged elastic band method for finding saddle points and minimum energy paths, *J. Chem. Phys.* 113 (2000) 9901–9904.
- [32] H. Zhang, Y. Li, J. Hou, K. Tu, Z. Chen, FeB₆ monolayers: The graphene-like material with hypercoordinate transition metal, *J. Am. Chem. Soc.* 138 (2016) 5644–5651.
- [33] L.-M. Yang, V. Bačić, I.A. Popov, A.I. Boldyrev, T. Heine, T. Frauenheim, E. Ganz, Two-dimensional Cu₂Si monolayer with planar hexacoordinate copper and silicon bonding, *J. Am. Chem. Soc.* 137 (2015) 2757–2762.
- [34] Y. Xu, B. Yan, H.-J. Zhang, J. Wang, G. Xu, P. Tang, W. Duan, S.-C. Zhang, Large-gap quantum spin hall insulators in tin films, *Phys. Rev. Lett.* 111 (2013) 136804.
- [35] L. Chen, Z. Chen, Y. Wang, C. Yang, Q. Jiang, Design of dual-modified MoS₂ with nanoporous Ni and graphene as efficient catalysts for the hydrogen evolution reaction, *ACS Catal.* 8 (2018) 8107–8114.
- [36] B. Hinnemann, P.G. Moses, J. Bonde, K.P. Jørgensen, J.H. Nielsen, S. Hørch, I. Chorkendorff, J.K. Nørskov, Biomimetic hydrogen evolution: MoS₂ nanoparticles as catalyst for hydrogen evolution, *J. Am. Chem. Soc.* 127 (2005) 5308–5309.
- [37] C. Ling, Y. Ouyang, L. Shi, S. Yuan, Q. Chen, J. Wang, Template-grown MoS₂ nanowires catalyze the hydrogen evolution reaction: Ultralow kinetic barriers with high active site density, *ACS Catal.* 7 (2017) 5097–5102.
- [38] T. Liao, L. Kou, A. Du, Y. Gu, Z. Sun, Simplest MOF units for effective photodriven hydrogen evolution reaction, *J. Am. Chem. Soc.* 140 (2018) 9159–9166.
- [39] D. Er, H. Ye, N.C. Frey, H. Kumar, J. Lou, V.B. Shenoy, Prediction of enhanced catalytic activity for hydrogen evolution reaction in janus transition metal dichalcogenides, *Nano Lett.* 18 (2018) 3943–3949.
- [40] J.K. Nørskov, T. Bligaard, A. Logadottir, J.R. Kitchin, J.G. Chen, S. Pandalov, U. Stimming, Trends in the exchange current for hydrogen evolution, *J. Electrochem. Soc.* 152 (2005) J23–J26.
- [41] A. Mahata, K.S. Rawat, I. Choudhuri, B. Pathak, Single-layered platinum nanocage: A highly selective and efficient catalyst for fuel cells, *J. Mater. Chem. A* 4 (2016) 12756–12767.
- [42] X. Zhang, A. Chen, Z. Zhang, M. Jiao, Z. Zhou, Transition metal anchored C₂N monolayers as efficient bifunctional electrocatalysts for hydrogen and oxygen evolution reactions, *J. Mater. Chem. A* 6 (2018) 11446–11452.
- [43] J.A. Keith, G. Jerkiewicz, T. Jacob, Theoretical investigations of the oxygen reduction reaction on Pt (111), *ChemPhysChem* 11 (2010) 2779–2794.
- [44] K. Li, Y. Li, Y. Wang, F. He, M. Jiao, H. Tang, Z. Wu, The oxygen reduction reaction on Pt (111) and Pt (100) surfaces substituted by subsurface Cu: A theoretical perspective, *J. Mater. Chem. A* 3 (2015) 11444–11452.
- [45] Y. Sha, T.H. Hu, B.V. Merinov, P. Shirvanian, W.A. Goddard, Oxygen hydration mechanism for the oxygen reduction reaction at Pt and Pd fuel cell catalysts, *J. Phys. Chem. Lett.* 2 (2011) 572–576.
- [46] Z. Duan, G. Wang, A first principles study of oxygen reduction reaction on a Pt (111) surface modified by a subsurface transition metal M (M = Ni, Co, or Fe), *Phys. Chem. Chem. Phys.* 13 (2011) 20178–20187.
- [47] Y. Wang, Y. Li, T. Heine, PtTe monolayer: Two-dimensional electrocatalyst with high basal plane activity towards oxygen reduction reaction, *J. Am. Chem. Soc.* 140 (2018) 12732–12735.
- [48] J. Liu, M. Jiao, L. Lu, H.M. Barkholtz, Y. Li, Y. Wang, L. Jiang, Z. Wu, D.-J. Liu, L. Zhuang, C. Ma, J. Zeng, B. Zhang, D. Su, P. Song, W. Xing, W. Xu, Y. Wang, Z. Jiang, G. Sun, High performance platinum single atom electrocatalyst for oxygen reduction reaction, *Nat. Commun.* 8 (2017) 15938.